

Ab-initio theory of metal-insulator interfaces in a finite electric field

Massimiliano Stengel¹ and Nicola A. Spaldin¹

¹*Materials Department, University of California, Santa Barbara, CA 93106-5050, USA*

(Dated: October 8, 2018)

We present a novel technique for calculating the dielectric response of metal/insulator heterostructures. This scheme allows, for the first time, the fully first-principles calculation of the microscopic properties of thin-film capacitors at finite bias potential. The method can be readily applied to pure insulators, where it provides an interesting alternative to conventional finite-field techniques based on the Berry-phase formalism. We demonstrate the effectiveness of our method by performing comprehensive numerical tests on a model Ag/MgO/Ag heterostructure.

PACS numbers: 71.15.-m

I. INTRODUCTION

The dielectric response of a metal-insulator interface to an applied electric field is a subject of great interest nowadays, as the ongoing miniaturization of electronic devices is reaching the atomic scale. In this regime, the properties of thin oxide films (used e.g. in nonvolatile ferroelectric memories¹ and as gate oxides in MOSFET transistors²) start to deviate from those predicted by macroscopic models, and cannot be disentangled from the metallic or semiconducting contact³. Traditionally, deviations from bulk dielectric behavior in thin film geometries have been described using phenomenological models, which have provided valuable insights into the *qualitative* consequences of low dimensionality and interfacing to a metallic electrode. However, such models do not have predictive *quantitative* capabilities for the many physical factors, such as interface chemistry⁴, finite screening length in the metal⁵, or the presence of structural and point defects related to the growth process, that contribute to the observed properties. In order to separate these effects and to help improve over the existing models, the electronic and ionic response of a metal-insulator heterostructure to an external bias potential must be understood at the quantum mechanical level.

First-principles calculations, especially within the framework of density functional theory, have proven to be a powerful tool in the fundamental understanding of metal-ceramic interfaces⁶. On the other hand, *ab-initio* studies of interfacial dielectric properties are still in their infancy, and only *insulating* heterostructures have been successfully simulated⁴ in a finite external field. Indeed, when one of the two materials is a metal (as required for the simulation of a realistic thin-film capacitor), the presence of partially filled bands at the Fermi level prevents the straightforward application of the Berry-phase technique⁷, on which most finite electric field calculations have been based so far^{8,9}. In order to gain further insight into the rich domain of phenomena occurring at metal-dielectric junctions there is the clear need for a methodology that allows one to work around this obstacle.

In this work we demonstrate how this problem can be solved by using techniques and ideas borrowed from Wannier-function theory, which is an appealing alternative to the traditional Berry-phase formalism¹⁰. In particular, we show that the insulating nature of a capacitor under an applied bias potential is reflected at the microscopic level in the confinement of the metal-induced gap states, whose propagation in the insulator is forbidden; this property allows for a rigorous definition of the macroscopic polarization in real space. The coupling to an external field is then introduced through the usual definition of the electric enthalpy, in close analogy to purely insulating systems^{8,9}.

We demonstrate the effectiveness of our technique using a model MgO/Ag(100) heterostructure; the simple properties of this well studied metal-ceramic interface make it an ideal test case for our method. In addition to providing a technical validation to our approach, our results indicate that MgO films retain an ideal classical behavior in the ultrathin limit, corroborating the picture that emerged from previous investigations¹¹.

This work is organized as follows. In Section II we define the polarization, the electric enthalpy and the Hamiltonian for our new finite-field approach, and show how it can be used to calculate the capacitance and local permittivity profiles of a general metal/insulator heterostructure. In Section III we relate our scheme to other possible approaches. In Section IV we present the numerical test on Ag/MgO in full detail, with particular focus on the new properties of the system that are made accessible by our scheme (dynamical charges at the interface, electronic response, etc.). In Section V we briefly discuss the applicability of our method to range of physical problems, and present the summary and conclusions.

II. METHOD

To place our developments in context, we begin by reviewing the discrete Berry-phase formalism introduced by King-Smith and Vanderbilt⁷ (KSV) for a general insulating crystal; we then adapt the method we developed in Ref. 12 to obtain a real-space expression for the polarization. Next (Sec. II B) we show how this procedure can be

readily extended to periodic metal/insulator heterostructures. Finally, in Sec. II C we introduce the coupling to an external field in the total energy and the Hamiltonian, which completes the derivation of our finite-field method. A discussion of the first-principles capacitance per unit area is provided in Sec. II D, and links our method to the theory of local permittivity¹³, which was originally developed for purely insulating heterostructures.

A. Insulating systems

We start with a periodic insulator described by three real space lattice vectors \mathbf{R}_i ; for convenience, we impose that $\mathbf{R}_1 = (a, 0, 0)$ is perpendicular to $\mathbf{R}_{2,3}$ (the latter two lie therefore on the yz plane). The Brillouin zone for such a Bravais lattice is a prism in reciprocal space defined by the reciprocal space vectors $\mathbf{G}_1 = (2\pi/a, 0, 0)$ and $\mathbf{G}_{2,3}$. We choose a discrete k -point sampling of the type $\mathbf{k} = j\mathbf{b} + \mathbf{k}_\perp$, where the vector \mathbf{b} , parallel = $(2\pi/L, 0, 0) = \mathbf{G}_1/N_\parallel$ spans a regular one-dimensional mesh of dimension $N_\parallel = L/a$ and \mathbf{k}_\perp belongs to a set of N_\perp special points in the perpendicular plane; the total number of independent k -points is then $N_\perp N_\parallel$. The x component of macroscopic polarization $\langle P \rangle$ is commonly evaluated on this reciprocal space mesh by first defining a set of matrices:

$$M_{mn}^{\mathbf{k}} = \langle u_{m\mathbf{k}} | u_{n\mathbf{k} + \mathbf{b}_\parallel} \rangle, \quad (1)$$

where it is understood that $|u_{n\mathbf{k} + \mathbf{G}_\parallel}\rangle = e^{-i\mathbf{G}_\parallel \mathbf{r}} |u_{n\mathbf{k}}\rangle$. In the KSV approach⁷ $\langle P \rangle$ is then calculated as a discrete Berry phase for each individual ‘‘stripe’’ of k -points:

$$\langle P \rangle_{Berry}(\mathbf{k}_\perp) = -\frac{2e}{\Omega} \frac{a}{2\pi} \sum_j \text{Im} \ln \det M^{\mathbf{k}_\perp + j\mathbf{b}}; \quad (2)$$

the resulting values are finally averaged over the set of special points \mathbf{k}_\perp with corresponding weights $w_{\mathbf{k}_\perp}$:

$$\langle P \rangle_{Berry} = \sum_{\mathbf{k}_\perp} w_{\mathbf{k}_\perp} \langle P \rangle_{Berry}(\mathbf{k}_\perp). \quad (3)$$

As an alternative, within single-particle theories, the macroscopic polarization can be equivalently related to the centers of the Wannier functions⁷. In Ref. 12 we have introduced a two-step procedure to obtain accurate values of the polarization by using a real-space technique based on Wannier functions:

- First, the maximally localized Wannier functions¹⁴ are determined iteratively starting from a set of ground-state Bloch orbitals;
- Then, the charge distribution of the Wannier function is constructed in real space, and the center defined by a saw-tooth function.

In the following, we modify this strategy to operate in one dimension instead of three, for several reasons: i) this

way we can achieve an even more transparent analogy between the Wannier-function real-space method and the KSV Berry-phase formula; ii) an external field couples to one component of the polarization only; iii) it can be generalized in a very natural way to a system which is at the same time a two-dimensional conductor and a one-dimensional insulator (see Section II B).

When the first step above is restricted to one dimension only, the resulting ‘‘hermaphrodite’’ Wannier functions^{13,15} are maximally localized along the x direction and Bloch-like in the orthogonal yz plane and are much easier to obtain compared to their three-dimensional counterparts. In fact, the unitary transformation that yields such a set of localized orbitals is constructed by means of the parallel-transport technique in a one-shot singular value decomposition, without the need for the iterative minimization of the spread functional¹⁴. The parallel transport technique consists¹⁴ of enforcing the particular representation of the orbitals in which $M_{mn}^{\mathbf{k}} = K_{mn}^{\mathbf{k}} \lambda_n^{\mathbf{k}_\perp}$, where $\lambda_n^{\mathbf{k}_\perp}$ are complex numbers of the form $\lambda_n^{\mathbf{k}_\perp} = e^{i\phi_n}$ and $K^{\mathbf{k}}$ is Hermitian. A definition of the Wannier centers can be written in terms of the phases ϕ_n :

$$\bar{x}_n^{\mathbf{k}_\perp} = \frac{aN_\parallel}{2\pi} \phi_n. \quad (4)$$

Interestingly, this definition of the centers of the parallel-transported hermaphrodite Wannier functions bears an exact relationship with the KSV *discrete* Berry-phase polarization:

$$\langle P \rangle_{Berry}(\mathbf{k}_\perp) = \frac{2e}{\Omega} \sum_n \bar{x}_n^{\mathbf{k}_\perp}. \quad (5)$$

Once the approximate values, $\bar{x}_n^{\mathbf{k}_\perp}$, of the Wannier centers are available, the ‘‘refinement’’ in real space by means of saw-tooth functions (second step above) can be carried out in close analogy to Ref. 12. First, the charge density associated with the hermaphrodite Wannier function $|w_{n\mathbf{k}_\perp}\rangle$ is explicitly constructed in a supercell which is a multiple of the primitive one (of total length L along x) and integrated over the yz planes to yield a one-dimensional function of periodicity L :

$$\rho_n^{\mathbf{k}_\perp}(x) = \int dydz |w_n^{\mathbf{k}_\perp}(\mathbf{r})|^2, \quad (6)$$

Then, the refined Wannier centers x_n are defined as:

$$x_n^{\mathbf{k}_\perp} = \int_{\bar{x}_n^{\mathbf{k}_\perp} - L/2}^{\bar{x}_n^{\mathbf{k}_\perp} + L/2} x \rho_n^{\mathbf{k}_\perp}(x) dx. \quad (7)$$

Finally, the expression for the polarization $\langle P \rangle$ follows:

$$\langle P \rangle(\mathbf{k}_\perp) = \frac{2e}{\Omega} \sum_n x_n^{\mathbf{k}_\perp}. \quad (8)$$

The advantages of using the real-space refinement step described above are twofold:

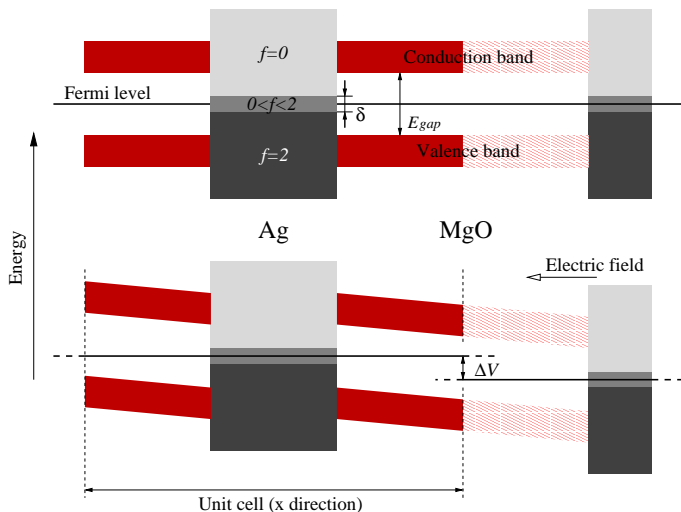


FIG. 1: Schematic representation of the projected band structure of a metal-insulator heterostructure in the absence of (top) and with (bottom) electric field. An effective bias potential ΔV between one slab and the repeated images is obtained.

- The real-space centers $x_n^{\mathbf{k}_\perp}$ are identical to the Berry-phase centers $\bar{x}_n^{\mathbf{k}_\perp}$ in the limit of $N_\parallel \rightarrow \infty$, but for a discrete mesh they differ; in particular, $x_n^{\mathbf{k}_\perp}$ converge *exponentially* to the asymptotic limit, while $\bar{x}_n^{\mathbf{k}_\perp}$ have a much slower, polynomial convergence (as $\mathcal{O}(N_\parallel^{-2})$)¹². Therefore in practice a relatively coarse k -point mesh is sufficient for the calculation of P , with a significantly reduced computational effort.
- The real-space expression for the polarization allows for a straightforward extension to metal/insulator heterostructures and the introduction of the coupling to a finite external field, which is the main goal of this work and will be treated in depth in the next subsection.

B. Metal/insulator heterostructures

We remind the reader that, in a metal/insulator heterostructure, the usual reciprocal-space expression for $\langle P \rangle$ based on the Berry phase is incompatible with the fractional orbital occupancies which stem from the metallicity of the electrodes; however, we will show hereafter that the real-space expression of the polarization described above can be adapted to provide a rigorous description also in this case. We start from the same assumptions and definitions as in the insulating case, except that we set $N_\parallel = 1$, i.e. only the two-dimensional special-points average on \mathbf{k}_\perp is performed in the Brillouin zone sampling. This is by no means a limitation, since for a physically meaningful study of a polarized capacitor a necessary condition is that there be no coupling

between the electrodes across the dielectric film, i.e. the corresponding one-particle bands must be virtually dispersionless along the x direction.

Incidentally, we note that “hermaphrodite” WFs, which are the basic ingredient of the method, are ideally suited to representing the inherently delocalized nature of electrons in the two-dimensionally conducting plates, while providing a fast spatial decay (which is crucial to an accurate definition of $\langle P \rangle$)¹² along the field direction (x). Unfortunately, the “localization” transformation, upon which the real-space formulation is rooted, cannot be performed straightforwardly here because of the fractional occupancies at the Fermi level: in the finite-temperature functional the total energy is no longer invariant upon a unitary transformation of the occupied states¹⁶. To work around this problem and achieve a localized representation along x , we divide the problem into three regimes, which (as above) are identified independently for every \mathbf{k}_\perp point of the surface Brillouin zone (a schematic representation is shown in Fig. 1):

- The conduction states with zero occupancy are discarded from the computation, since they do not contribute to the ground state energy or charge density.
- The submanifold of fully occupied valence states (with energy eigenvalue $\epsilon_n < E_F - \delta$ in Fig. 1) is localized separately by means of the parallel-transport algorithm^{14,17}; this operation leaves the total energy unaffected in complete analogy to the purely insulating case.
- The partially occupied states in the region of the Fermi level (shown as “ $0 < f < 2$ ” in Figure 1) lie in the energy gap of the dielectric; as a result they are quantum mechanically confined in the metallic slab without taking any further action, since they cannot propagate through the insulator.

The centers, $x_n^{\mathbf{k}_\perp}$, of the resulting set of localized orbitals are then calculated, analogously to the insulating case, by using Eq. 7 (for the metal-induced gap states we set $\bar{x}_n = 0$ and assume by convention that the metallic slab is approximately centered at $x = 0$). The definition of the polarization is identical to the insulating case, except that we must take the orbital occupation numbers $f_n^{\mathbf{k}_\perp}$ explicitly into account:

$$\langle P \rangle(\mathbf{k}_\perp) = \frac{e}{\Omega} \sum_n f_n^{\mathbf{k}_\perp} x_n^{\mathbf{k}_\perp}. \quad (9)$$

The multi-valuedness in the definition of $x_n^{\mathbf{k}_\perp}$ (modulo a lattice vector) is removed by imposing $x_n^{\mathbf{k}_\perp} \in [-L/2, L/2]$, with the origin $x = 0$ corresponding to the center of the metallic slab and L the cell length³⁵. Since the band energies change their value during structural relaxation, the whole procedure has to be repeated at the beginning of every iteration. This means that the number of states assigned to each energy window is not

fixed during the simulation, but is free to vary, following the evolution of orbital eigenvalues.

We note that the exact boundaries of the energy windows, in particular the energy separating the orbitals that are considered metal-induced gap states and those that are localized by means of the parallel-transport procedure, is to some extent arbitrary; this choice, however, has no influence on the result (provided that in the lower window all states are fully occupied and that the middle window does not overlap with the conduction or valence band of the insulator). The method is therefore well defined.

C. Electric enthalpy and Hamiltonian

The coupling of a periodic system to a finite external field \mathcal{E} is described, in both the metallic and insulating cases, by the electric enthalpy^{8,9}:

$$E^{\mathcal{E}} = E_{KS} - \Omega \mathcal{E} \cdot \langle P \rangle, \quad (10)$$

where E_{KS} is the Kohn-Sham total energy, Ω is the volume of the supercell and $\langle P \rangle$ is the macroscopic polarization along the field axis; in a parallel-plate capacitor this is always perpendicular to the electrode plane.

We write the contribution $\Delta \hat{H}^{\mathcal{E}}$ to the Hamiltonian due to the electric field operator as a non-local, state-dependent potential $F_n(x)$ applied to each WF, w_n , individually (we drop the superscript \mathbf{k}_{\perp} in the following discussion):

$$\Delta \hat{H}^{\mathcal{E}} = \mathcal{E} \sum_n |\hat{F}_n w_n\rangle \langle w_n|. \quad (11)$$

The $F_n(\mathbf{r})$ are periodic sawtooth functions³⁶ of the form $F_n(\mathbf{r}) = x$, with $x \in [x_n - L/2, x_n + L/2]$, i.e. $F_n(0, y, z) = 0$ for every n , and is discontinuous in a point located far from the center x_n , where the corresponding orbital has vanishing importance. We note that the average value of $F_n(x)$ over the cell is irrelevant for a purely insulating system, but is crucial when a metallic electrode is present. It can be easily verified that our choice respects the correct limit in the case of an isolated metallic slab in vacuum, where the field operator becomes *local*. This also means that, when a center x_n crosses the point $x = L/2$ (the center of the insulating slab), the corresponding polarizing potential $\mathcal{E}F_n(x)$ undergoes a discontinuous, rigid jump of magnitude $\Delta V = \pm \mathcal{E}L$. For a sufficiently thick insulating layer, and as long as ΔV is small enough not to bring valence or conduction states into the partially occupied region close to the Fermi level, this jump leaves the system unaffected apart from a trivial shift of the eigenvalues corresponding to fully-occupied Bloch states (the discontinuity can also be effectively smoothed by smearing the F_n with Gaussian functions; a practical procedure to do this is explained in the Appendix). Interestingly, the large-field Zener instability reported for purely insulating

bulk materials^{8,9} translates here to a *Schottky-tunneling* instability that has to be avoided by careful analysis of the band alignment.

$\Delta \hat{H}^{\mathcal{E}}$ has in general a small anti-Hermitian part due to the fact that the Wannier functions are never exactly zero at the cell boundary but retain a small (exponentially vanishing) tail:

$$\langle w_i | \Delta \hat{H}^{\mathcal{E}} | w_j \rangle - (\langle w_j | \Delta \hat{H}^{\mathcal{E}} | w_i \rangle)^* = \langle w_i | (F_j - F_i) | w_j \rangle.$$

The influence of this anti-Hermitian component is to induce a ‘‘unitary torque’’ within the manifold of the occupied orbitals, which is undesirable since, when working in the ensemble density functional theory framework (or even more clearly in the case of insulating systems), the total energy (and the electric enthalpy) are both invariant with respect to such a unitary transformation; this is therefore a spurious contribution that we remove by introducing a correction term of the form:

$$\Delta \hat{H}' | w_i \rangle = \frac{\mathcal{E}}{2} \sum_j | w_j \rangle \langle w_j | (F_j - F_i) | w_i \rangle. \quad (12)$$

This term goes exponentially to zero with increasing insulator thickness, and vanishes if each Wannier-like state is strictly localized in $x \in [x_n - L/4, x_n + L/4]$. With this correction, we could always achieve optimal convergence to the electronic ground state.

We want to stress here that, at the origin of the non-zero anti-Hermitian term (Eq. 12), there’s an important *physical* feature, i.e. the tunneling current across a thin insulating film is never exactly zero (although it is exponentially decreasing as a function of film thickness). In order to study the metastable (long-lived) state of the polarized capacitor within a ground-state theory, we are obliged to make an approximation and discard the tunneling current by truncating the tails of the evanescent conduction states induced by the metallic electrodes. We expect this approximation to be very good in cases where the tunneling current is so negligibly small that it does not contribute appreciably to the physics of the system. This condition is indeed satisfied in the regime where our method is exact, i.e. when the tails of the metal-induced gap states are confined to a region much smaller than the thickness of the insulating film, and therefore direct tunneling is suppressed.

D. Local dielectric response and capacitance

The theory of local permittivity that was originally developed for purely insulating interfaces¹³ is directly applicable to metal/insulator heterostructures, and can be readily generalized to introduce the first-principles capacitance density per unit area, \mathcal{C} . We start from the usual textbook definition of the capacitance density,

$$\mathcal{C} = \frac{\sigma}{\Delta V}, \quad (13)$$

with $\Delta V = \mathcal{E}L$ the potential drop between the electrodes, and σ the surface density of the *free* charge stored in the device. From classical electrostatics, the free charge is equal to the value of the induced polarization deep inside the electrode, where the applied field is completely screened. In our geometry this occurs in the center ($x = 0$) of the metallic slab, and Eq. 13 can be rewritten as

$$C = \frac{\Delta \bar{P}(x=0)}{\mathcal{E}L}, \quad (14)$$

where $\Delta \bar{P}(x)$ is the planar- and macroscopically-averaged¹⁸ induced polarization. Finally, $\Delta \bar{P}(0)$ can be extracted from the relationship, derived in Ref. 13, between the local permittivity, $\bar{\epsilon}(x)$, and the induced polarization, and the corresponding globally averaged quantities $\langle \epsilon \rangle$ and $\langle \Delta P \rangle$:

$$\left(1 - \frac{1}{\bar{\epsilon}(x)}\right) = \left(1 - \frac{1}{\langle \epsilon \rangle}\right) \frac{\Delta \bar{P}(x)}{\langle \Delta P \rangle}. \quad (15)$$

Since deep in the metal $\bar{\epsilon}(x)$ diverges [i.e. $1/\bar{\epsilon}(0) = 0$], Eq. 15 reduces simply to $\Delta \bar{P}(x=0) = \langle \Delta P \rangle + \mathcal{E}/(4\pi)$, and Eq. 13 reduces to

$$C = \frac{\langle \epsilon \rangle}{4\pi L}, \quad (16)$$

where $\langle \epsilon \rangle = 4\pi \langle \Delta P \rangle / \mathcal{E} + 1$ is the overall dielectric constant of the supercell, and $\langle \Delta P \rangle$ is the polarization induced by the field \mathcal{E} . We use equation 16 to obtain the capacitance values in Section IV.

In order to appreciate the influence of the interface on the properties of the device, it is often interesting to compare the *ab-initio* value of the capacitance (Eq. 16) to the well-known classical formula, which is valid in the macroscopic regime and depends only on the thickness t and on the bulk permittivity of the dielectric film ϵ_{bulk} :

$$C_{classical} = \frac{\epsilon_{bulk}}{4\pi t}. \quad (17)$$

In a size regime comparable to the electronic wavelength the “thickness” of the insulating slab ceases to be a rigorous concept, since the transition from one bulk material to the other is not sharp, and their individual properties are strongly modified in close vicinity of the junction. In most cases we can define a “nominal” thickness as $t = mt_0$, where m is the number of layers of the crystalline film and t_0 is the equilibrium interlayer spacing of the dielectric film far from the interface. Together with this definition of the thickness, we will use Eq. 17 in Section IV to define a nominal capacitance C_0 .

III. ALTERNATIVE APPROACHES

A. Metal/insulator heterostructures

In principle, to address the problem of the dielectric transition at a metal/insulator interface, several alternatives to our method can be explored; we will briefly review in this section the most obvious solutions.

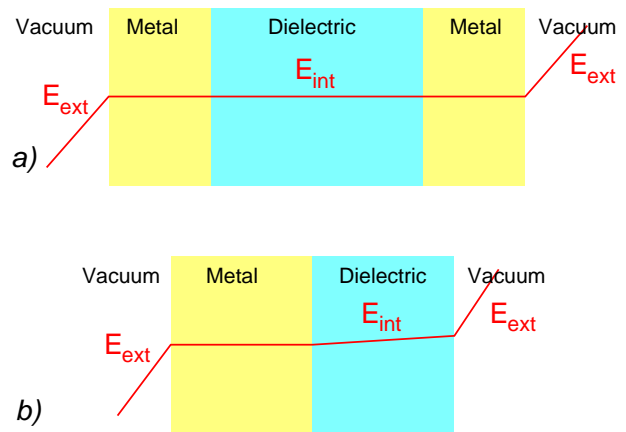


FIG. 2: Schematic representation of the self-consistent electrostatic potential (red curve) in unsupported metal/insulator/metal (a) and metal/insulator (b) slabs when an external field \mathcal{E}_{ext} is switched on. In the geometry (a) by classical electrostatics the internal macroscopic field acting on the dielectric \mathcal{E}_{int} is zero; in case (b) it corresponds to $\mathcal{E}_{ext}/\epsilon_{bulk}$, where ϵ_{bulk} is the bulk dielectric constant of the insulator.

We have already mentioned that the Berry phase formalism is difficult to apply because of the partially occupied states at the Fermi level. Conventional linear-response¹⁹ techniques seem also problematic, because the response to a uniform external field is again incompatible with the overall metallic character of the system. A promising alternative is provided by quantum transport techniques, either within the nonequilibrium Green’s function formalism or within time-dependent density functional theory²⁰; our approach should yield comparable results in the limit of small tunneling current, although probably at a substantially lower computational cost.

A different approach consists in introducing a layer of vacuum in the heterostructure, in order to allow for the straightforward application of a local saw-tooth potential; since a capacitor is a finite object this seems also a natural choice for the geometry (Fig. 2a). As the two electrodes lie in the same supercell, however, there is only one Fermi level that defines the chemical potential of an electron in both metallic slabs; in other words, an external perturbation can not induce a potential difference between the capacitor plates. Instead, the system behaves as a short circuit, analogously to a thick, homogeneous metallic slab, irrespective of the dielectric material sandwiched in between. In this case, the external field is completely screened by the accumulation/depletion of charge at the free surfaces of the conductor.

A possibility to work around this problem is to simulate just “half” of the capacitor, i.e. a metal/insulator slab isolated in vacuum (Fig. 2b). Again, an external saw-tooth function can be used both to apply a uniform external field and to define the polarization $\langle P \rangle$; from the self-consistent electronic ground state in this perturbed

potential we can extract charge density differences and local polarization profiles, that can then be used to estimate the capacitance and interfacial properties. There are, however, some limitations to this approach:

- The termination of the insulating lattice must not be metallic or we recover case 1 above; this rules out the simulation of most polar interfaces [e.g. (100)-oriented 5-1 or 3-3 perovskites]. Furthermore, even for “insulating” crystal surfaces, sometimes surface states due to dangling bonds substantially reduce the electronic gap, thus limiting the range of electric field values that can be used in practice.
- By classical electrostatics, the electric field in the vacuum is larger than the electric field in the insulator by a factor of ϵ . This means that, for high-permittivity dielectrics, simulations are restricted to extremely small values of the internal field, and therefore the non-linear regime is not practically accessible by means of this strategy. Even worse, when the insulator is a ferroelectric, it has already been shown that the presence of a free surface makes it difficult to impose the correct electrical boundary conditions inside the film²¹.

The advantage of our method is that its limitations are exclusively dictated by fundamental physics (Schottky or direct tunneling), not by artifacts that must be introduced *ad hoc* in an unconventional simulation cell. We note that the band alignment at the metal/dielectric junction plays a crucial role in determining the properties of the interface; particular care must be used to assess the reliability of the exchange and correlation functional in reproducing this feature, at least at a qualitative level.

B. Pure insulators

A real-space approach for applying a finite external field to a periodic system was first proposed by Nunes and Vanderbilt²² and applied to a tight-binding Hamiltonian, which was based on the linear-scaling scheme of Mauri, Galli and Car²³. The first application of this approach to a self-consistent density-functional calculation was presented by Fernández, Dal Corso and A. Baldereschi²⁴, and validated by the study of the dielectric properties of bulk Si and GaAs. The great advantage provided by the linear scaling functional (Ref. 23) is that it leads naturally to a description of the electronic structure in terms of Wannier functions which are strictly confined in space; this means that the real-space position operator is formally well-defined. The price to pay, however, is that one has to deal with a non-conventional functional, where the orthonormality constraint is not exactly satisfied and that might pose convergence problems during the search for the electronic ground state; we are not aware of practical follow-ups of these techniques.

The vast majority of the finite-field calculations reported so far were performed within the scheme of Souza,

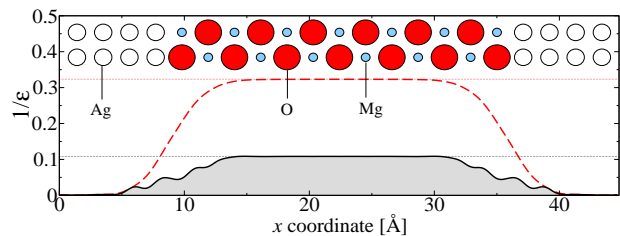


FIG. 3: High-frequency (red dashed curve) and static (black shaded curve) inverse permittivity profiles for the Ag/MgO heterostructure. Bulk values for the inverse permittivity are indicated as thin dotted lines. The approximate positions of the atomic planes are sketched in the upper part of the figure.

Íñiguez and Vanderbilt⁸ or Umari and Pasquarello⁹, both based on the Berry-phase definition of polarization. In the case of pure insulators, our scheme can be considered as an interesting practical alternative to the latter two approaches, since it can yield substantially better accuracy for the same choice of computational parameters.

IV. APPLICATION AND NUMERICAL TESTS

We demonstrate the effectiveness of our scheme by presenting results for a model $[\text{Ag}(100)]_n/[\text{MgO}(100)]_m$ heterostructure, with the thicknesses of the Ag and MgO slabs set to $n = 9$ and $m = 13$ atomic layers respectively. We choose to fix the in-plane lattice constant to our calculated equilibrium value of bulk MgO ($a_0 = 7.86$ a.u.), and apply a 3% uniform in-plane expansion to the Ag lattice in order to obtain a pseudomorphic structure. The O atoms are placed on top of the interface Ag atoms, which is the most favorable alignment; the interface Mg atoms then sit above a four-fold hollow site of the Ag(100) surface.

A. Computational parameters and zero-field equilibrium structure

Our calculations were performed within the local density approximation²⁵ and the PAW method²⁶ as implemented in our “in-house” code, with a plane wave cutoff of 40 Ry, a Gaussian smearing of 0.2 eV for the orbital occupancies and 10 special k -points in the surface Brillouin zone. For all electronic and ionic relaxations we used an extension of the Car and Parrinello²⁷ method to metallic systems^{28,29}. The out-of-plane atomic positions and cell parameter were relaxed in zero field until the maximum force was lower than 0.05 meV/Å, and the spacing t_0 between the central MgO layers was within 0.2% of the bulk equilibrium value.

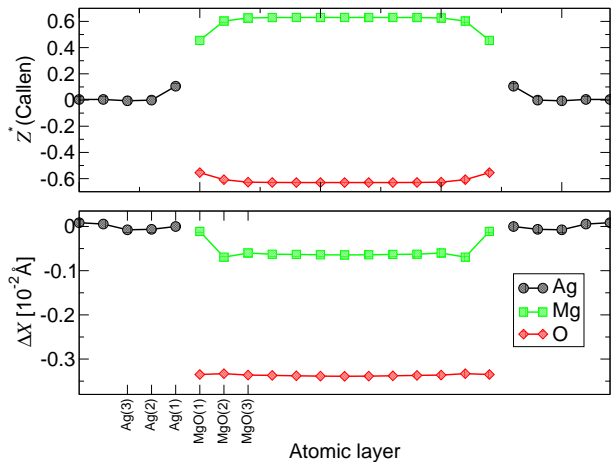


FIG. 4: (i) x (longitudinal) component of the Callen dynamical charges in the Ag/MgO heterostructure in units of e . (ii) Atomic relaxations induced by a field of 10^{-4} a.u.

B. High-frequency response

We then imposed an external field of $51.4 \text{ V}/\mu\text{m}$ and relaxed the electrons to the ground state while keeping the ions fixed. The resulting high-frequency permittivity profile is shown as a thick dashed curve in Fig. 3. On the metal side of the interface the inverse permittivity drops quickly to zero, as expected, while it is very close to our calculated bulk MgO value after only three atomic layers on the insulator side (the bulk calculations were performed on a tetragonal 8-layer non-primitive supercell with the same in-plane lattice parameter and k -point sampling as the interface system; the out-of-plane spacing was set to t_0). The calculated value in the middle of the MgO slab is $\bar{\epsilon}^\infty(L/2)=3.095$, which is within 0.03% of our calculated bulk value, $\epsilon_{bulk}^\infty=3.094$. This level of accuracy reflects the favorable convergence of the real-space expression of the polarization, which was demonstrated in Ref. 12. As a comparison, in a previous calculation of insulating heterostructures based on the Berry-phase approach, errors introduced solely by the finite field formalism were estimated to be of the order of 10%¹³. The overall dielectric constant of the heterogeneous supercell was $\langle \epsilon^\infty \rangle = 5.203$.

C. Dynamical charges

The ionic forces f_I extracted from the finite-field ground state calculation provide the Born effective charges $Z_I^* = f_I/\mathcal{E}$ of all atoms at once⁹; their values, however, are not a local property of the interface as they depend on the overall geometry and composition of the supercell. It is physically more insightful, instead, to look at the Callen (or longitudinal) dynamical charges, which are obtained by dividing the Born charges by the average high-frequency dielectric constant of the heterostructure

Layer	Z^* (Callen)
Ag(4)	0.004
Ag(3)	-0.006
Ag(2)	-0.001
Ag(1)	0.106
MgO(1)	0.455, -0.554
MgO(2)	0.603, -0.608
MgO(3)	0.626, -0.627
MgO(4)	0.629, -0.629
Bulk MgO	0.630, -0.630

TABLE I: Callen dynamical charges at the MgO/Ag(100) interface; in MgO the first values refers to Mg, the second to O.

$\langle \epsilon^\infty \rangle$, and are indeed local³⁰. The Callen charges for the present system are represented in the upper panel of Fig. 4; their values for the atoms closest to the interface are reported in Tab. I. It is apparent that, already three or four layers away from the interface, the charges associated to the Mg and O ions have already converged to the bulk value; their absolute value is slightly reduced in the first two MgO layers, while at the same time the interfacial Ag atom has a non-negligible positive charge. This behavior is consistent with the penetration of the metallic states in the insulator, which partially screens the ionic response of the ions closest to the interface; at the same time, the external field has a finite penetration length in the metallic slab, which affects the interface Ag layer.

D. Static response

The ionic contribution to the static polarization can be either evaluated in the linear (zero field) approximation with standard linear-response techniques¹⁹, or non-perturbatively, by performing a direct relaxation in a finite external field⁹; we tested both approaches here. First we computed the symmetry-restricted force matrix of the system by the finite-difference method in zero field using small displacements of 0.0004 \AA along x . The variation of the *local* polarization upon atomic displacements, $\delta P(x, \{R_I\})/\delta R_I$, was also simultaneously extracted for each degree of freedom and used, together with the force matrix and the Born effective charges, to construct the static permittivity profile, $\bar{\epsilon}^0(x)$, which is shown as a thick solid curve in Fig. 3. The behavior of the static and high frequency permittivities are similar, the only relevant difference being their magnitudes in the middle of the insulating slab, with $\bar{\epsilon}^0(L/2)$ converging to a value of 9.227 (our calculated $\epsilon_{bulk}^0 = 9.229$). In the lower panel of Fig. 4 we show the field-induced atomic displacements (the center of the metallic slab has been assumed as a reference). As expected, the metallic slab remains practically unperturbed, while interestingly, with this choice

of origin, both Mg and O sublattices relax opposite to the field direction; the relaxation of the Mg ions is much less important than the relaxation of the oxygens.

Next, we performed a direct relaxation of the atomic positions in an external bias $\Delta V = 1.15$ V, which corresponds roughly to a self-consistent field of 400 V/ μm throughout the dielectric; the resulting average permittivity was within 0.05% of the zero field linear response value, indicating as expected the absence of anharmonic effects in this field regime within numerical accuracy.

E. Capacitance density

Having assessed the reliability of our technique, and obtained accurate profiles, we next extracted the static and high-frequency values of the capacitance, obtaining $C^0 = 31.2$ fF/ μm^2 and $C^\infty = 10.3$ fF/ μm^2 respectively. These values are respectively 3.1% and 1.2% higher than the classical estimates based only on the knowledge of the bulk permittivity and of the thickness of the film:

$$C_{classical}^{(0,\infty)} = \frac{\epsilon_{bulk}^{(0,\infty)}}{4\pi m t_0} \quad (18)$$

The close similarity between C and $C_{classical}$ indicates that the influence of the metal on the dielectric properties of the MgO film is very small. Previous investigations of ultrathin MgO films deposited on Ag have already evidenced a surprisingly fast recovery of the bulk oxide local electronic structure as a function of film thickness¹¹; here we see that this result also holds for the *dielectric* properties of MgO films, which show a nearly ideal classical behaviour down to the nanometer scale.

F. Molecular dynamics

Since the formalism is not exactly variational, it is important to assess its suitability for calculating finite-temperature effects by monitoring energy conservation during a microcanonical molecular dynamics run²⁸. We start from the centrosymmetric zero-field equilibrium structure and let the atoms evolve along the x axis under an external bias of $\Delta V = 1.15$ V. The evolution of the potential energy $E^\mathcal{E}$, of the “physical” constant of motion $E^\mathcal{E} + K_{ion}$ and of the approximate “mathematical” constant of motion $E^\mathcal{E} + K_{ion} + K_{fake}$ (K_{ion} is the ionic kinetic energy, while K_{fake} is the fictitious electronic kinetic energy²⁷) are shown in the upper panel of Fig. 5. The quality of the energy conservation is excellent; the curve has no appreciable drift, even when enlarging the vertical scale by three orders of magnitude. In the lower panel we show the evolution of $\langle P \rangle$, which undergoes quasiperiodic oscillations of approximate frequency 390 cm^{-1} . To link the molecular dynamics run to the lattice-dynamical properties of the system extracted from the force matrix, in the inset we show the phonon

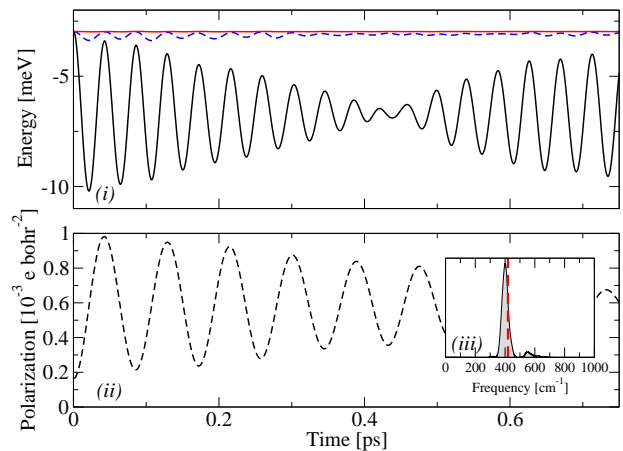


FIG. 5: (i) Energy conservation during molecular dynamics in an external bias of 1.15 V. Represented are $E^\mathcal{E}$ (black solid), $E^\mathcal{E} + K_{ion}$ (blue dashed) and $E^\mathcal{E} + K_{ion} + K_{fake}$ (red solid). The zero of the energy scale is set at the ground state total energy in zero field. (ii) Polarization, $\langle P \rangle$, as a function of time. (iii) Frequency-resolved dipolar activity of the system (black shaded curve); zone-center transverse optical phonon frequency of bulk MgO is also shown (red dashed line).

spectrum broadened by a Gaussian of width 20 cm^{-1} and weighted by the dipolar activity of the mode, $[Z^*(\omega)]^2$, where $Z^*(\omega)$ is the mode effective charge³¹. The dominant peak, centered at 400 cm^{-1} , closely corresponds to the main oscillation period of the polarization $\langle P \rangle$ during the dynamics; the frequency of the calculated zone-center transverse optical mode of bulk MgO (420 cm^{-1}) is indicated as a thick dashed line.

V. CONCLUSIONS

In summary, we have developed a first-principles method for calculating the response of hybrid metal/insulator structures to an electric field, and have demonstrated its applicability by calculating the local permittivity and capacitance of a model thin-film capacitor. The method is also appropriate for insulating materials at finite bias, where it provides greater accuracy than conventional techniques, in both the linear and anharmonic regimes with respect to field and temperature; this is crucial in the simulation of ferroelectric devices, where anharmonic effects are an essential physical ingredient for a realistic description³¹. The generality of the technique is evidenced by the high quality of overall energy conservation in molecular dynamics, which suggests fascinating applications to phenomena occurring at liquid/electrode interfaces, e.g. the recently observed freezing of interfacial water under electric fields³².

This work was supported by the National Science Foundation’s Division of Materials Research through the Information Technology Research program, grant num-

ber DMR-0312407, and made use of MRL Central Facilities supported by the National Science Foundation under award No. DMR-0080034

APPENDIX A: NUMERICAL IMPLEMENTATION

In this Appendix we will describe the technical details of the implementation of our method within the projector-augmented wave²⁶ (PAW) formalism. The same prescriptions apply to the closely related ultra-soft pseudopotential technique³³, while the case of norm-conserving pseudopotentials is easily recovered by removing the augmentation terms in the following expressions.

1. Notation

The basic ingredients of the PAW method are a set of all-electron (AE) and pseudo (PS) partial waves, respectively $|\phi_{\tau,i}\rangle$ and $|\tilde{\phi}_{\tau,i}\rangle$, and the corresponding projector functions $|\tilde{p}_{\tau,i}\rangle$. The index i here embeds three indices: two angular momentum variables l and m , and a third one, n , that accounts for the fact that several partial waves per angular momentum can be used; the dependence on the atomic species/site is included in τ . It is useful to define two kind of integrals based on these quantities, namely the overlap matrix elements:

$$Q_{\tau,ij} = \langle \phi_{\tau,i} | \phi_{\tau,j} \rangle - \langle \tilde{\phi}_{\tau,i} | \tilde{\phi}_{\tau,j} \rangle, \quad (\text{A1})$$

and the localized dipole moments of the augmented charges:

$$d_{\tau,ij} = \langle \phi_{\tau,i} | x | \phi_{\tau,j} \rangle - \langle \tilde{\phi}_{\tau,i} | x | \tilde{\phi}_{\tau,j} \rangle. \quad (\text{A2})$$

Most of these integrals are zero because of the angular momentum selection rules. The projectors are used to construct the local density matrices:

$$W_{\tau,ij} = \sum_{\mathbf{n}\mathbf{k}} f_{\mathbf{n}\mathbf{k}} \langle \psi_{\mathbf{n}\mathbf{k}} | \tilde{p}_i \rangle \langle \tilde{p}_j | \psi_{\mathbf{n}\mathbf{k}} \rangle \quad (\text{A3})$$

2. Polarization

Next, following Ref. 34 we first separate the total polarization into three parts:

$$P = P_{ion} + P^{BP} + P^{EV}, \quad (\text{A4})$$

respectively the ionic contribution, the Berry phase (BP) contribution and the expectation value (EV) term. The first is trivial, and is given by the dipole moment of the bare pseudo-atomic charges:

$$P_{ion} = \frac{e}{\Omega} \sum_{\tau} Q_{\tau} X_{\tau}. \quad (\text{A5})$$

The third (EV) term is also easy to compute and is nothing but the total dipole moment of the augmented charges:

$$P^{EV} = -\frac{e}{\Omega} \sum_{\tau,ij} d_{\tau,ij} W_{\tau,ij}. \quad (\text{A6})$$

The second (BP) term has the same form as Eq. 2:

$$\langle P \rangle_{Berry}^{BP}(\mathbf{k}_{\perp}) = -\frac{2e}{\Omega} \frac{a}{2\pi} \sum_j \text{Im} \ln \det M^{\mathbf{k}_{\perp} + j\mathbf{b}}; \quad (\text{A7})$$

however, the M matrix here must include the appropriate augmentation terms:

$$M_{mn}^{\mathbf{k}} = \langle u_{m\mathbf{k}} | u_{n\mathbf{k} + \mathbf{b}_{\parallel}} \rangle +$$

$$\sum_j Q_{\tau,ij} \langle u_{m\mathbf{k}} | \tilde{p}_i^{(\mathbf{k})} \rangle \langle \tilde{p}_j^{(\mathbf{k} + \mathbf{b}_{\parallel})} | u_{n\mathbf{k} + \mathbf{b}_{\parallel}} \rangle \quad (\text{A8})$$

The parallel transport construction explained in Sec. II A then provides the unitary rotations that localize the Wannier functions along the field axis, which lead easily to the one-dimensional PS Wannier densities $\tilde{\rho}_n(x)$. Within PAW, however, there is one supplementary step that must be taken when explicitly constructing the localized orbitals in real space, i.e. one must reconstruct the localized augmented charges associated with the Wannier orbital; in particular we will need in the following the *total* augmented charge per site associated to the n -th Wannier function:

$$q_{\tau,n} = \sum_{ij} Q_{\tau,ij} \langle w_n | \tilde{p}_i \rangle \langle \tilde{p}_j | w_n \rangle \quad (\text{A9})$$

3. Saw-tooth functions

Finally, to complete our definition of the polarization we need to construct the saw-tooth functions $F_n(x)$ in real space; in the following we present a recipe to do so while ensuring a continuous evolution of the Hamiltonian operator. Given a Wannier center w_n of approximate center \bar{x}_n (we always set $\bar{x}_n = 0$ for the metal-induced gap states with fractional orbital occupancies), defined in a one-dimensional cell of length L , we construct first the periodic function:

$$H_n(x) = 1 - A \sum_{l=-\infty}^{\infty} e^{-[x - \bar{x}_n + (l+1/2)L]^2 / \sigma^2} \quad (\text{A10})$$

where $A = L/(\sqrt{\pi}\sigma)$ is such that the average value of H is zero and σ is about 0.5-1 bohr. Then we define our saw-tooth function as the integral of H_n :

$$F_n(x) = \int_0^x H_n(y) dy \quad (\text{A11})$$

We note that this definition ensures that $F_n(0) = 0$ for all n ; the finite value of σ effectively avoids any discontinuity

in the evolution of the Hamiltonian while facilitating the plane-wave representation. Then the “refined” center x_n is defined as:

$$x_n = \int_0^L F_n(x) \tilde{\rho}_n(x) dx + \sum_{\tau} F_n(X_{\tau}) q_{\tau,n} + \bar{x}_n - F_n(\bar{x}_n), \quad (\text{A12})$$

where $q_{\tau,n}$ is the augmented charge at the atomic site τ associated with the n -th Wannier function, and X_{τ} is

the atomic position. Note that the charges $q_{\tau,n}$ and the PS densities satisfy the usual generalized normalization condition:

$$\int_0^L \tilde{\rho}_n(x) dx + \sum_{\tau} q_{\tau,n} = 1 \quad (\text{A13})$$

The $F_n(x)$ functions are then used in Eq. 11 to build the electric field contribution to the Hamiltonian.

-
- ¹ C. H. Ahn, K. M. Rabe, and J.-M. Triscone, *Science* **303**, 488 (2004).
- ² K. Eisenbeiser, J. M. Finder, Z. Yu, J. Ramdani, J. A. Curls, J. A. Hallmark, R. Droopad, W. J. Ooms, L. Salem, S. Bradshaw, et al., *Appl. Phys. Lett.* **76**, 1324 (2000).
- ³ M. Dawber, K. M. Rabe, and J. F. Scott, *Rev. Mod. Phys.* **77**, 1083 (2005).
- ⁴ F. Giustino, P. Umari, and A. Pasquarello, *Phys. Rev. Lett.* **91**, 267601 (2003).
- ⁵ J. Junquera and P. Ghosez, *Nature* **422**, 506 (2003).
- ⁶ M. W. Finnis, *J. Phys.: Condens. Matter* **8**, 5811 (1996).
- ⁷ R. D. King-Smith and D. Vanderbilt, *Phys. Rev. B* **47**, R1651 (1993).
- ⁸ I. Souza, J. Íñiguez, and D. Vanderbilt, *Phys. Rev. Lett.* **89**, 117602 (2002).
- ⁹ P. Umari and A. Pasquarello, *Phys. Rev. Lett.* **89**, 157602 (2002).
- ¹⁰ R. Resta, *J. Phys.: Condens. Matter* **14**, R625 (2002).
- ¹¹ S. Schintke, S. Messerli, M. Pivetta, F. Patthey, L. Libioulle, M. Stengel, A. De Vita, and W. D. Schneider, *Phys. Rev. Lett.* **87**, 276801 (2001).
- ¹² M. Stengel and N. A. Spaldin, *Phys. Rev. B* **73**, 075121 (2006).
- ¹³ F. Giustino and A. Pasquarello, *Phys. Rev. B* **71**, 144104 (2005).
- ¹⁴ N. Marzari and D. Vanderbilt, *Phys. Rev. B* **56**, 12847 (1997).
- ¹⁵ C. Sgierovello, M. Peressi, and R. Resta, *PRB* **64**, 115202 (2001).
- ¹⁶ N. Marzari, D. Vanderbilt, and M. C. Payne, *Phys. Rev. Lett.* **79**, 1337 (1997).
- ¹⁷ U. V. Waghmare, N. A. Spaldin, H. C. Kandpal, and R. Shadri, *Phys. Rev. B* **67**, 125111 (2003).
- ¹⁸ A. Baldereschi, S. Baroni, and R. Resta, *Phys. Rev. Lett.* **61**, 734 (1988).
- ¹⁹ S. Baroni, S. de Gironcoli, and A. D. Corso, *Rev. Mod. Phys.* **73**, 515 (2001).
- ²⁰ K. Burke, R. Car, and R. Gebauer, *Phys. Rev. Lett.* **94**, 146803 (2005).
- ²¹ B. Meyer and D. Vanderbilt, *Phys. Rev. B* **63**, 205426 (2001).
- ²² R. W. Nunes and D. Vanderbilt, *Phys. Rev. Lett.* **73**, 712 (1994).
- ²³ F. Mauri, G. Galli, and R. Car, *Phys. Rev. B* **47**, 9973 (1993).
- ²⁴ P. Fernández, A. Dal Corso, and A. Baldereschi, *Phys. Rev. B* **58**, R7480 (1998).
- ²⁵ J. P. Perdew and Y. Wang, *Phys. Rev. B* **45**, 13244 (1992).
- ²⁶ P. E. Blöchl, *Phys. Rev. B* **50**, 17953 (1994).
- ²⁷ R. Car and M. Parrinello, *Phys. Rev. Lett.* **55**, 2471 (1985).
- ²⁸ J. VandeVondele and A. De Vita, *Phys. Rev. B* **60**, 13241 (1999).
- ²⁹ M. Stengel and A. De Vita, *Phys. Rev. B* **62**, 15283 (2000).
- ³⁰ F. Giustino and A. Pasquarello, *Phys. Rev. Lett.* **95**, 187402 (2005).
- ³¹ A. Antons, J. B. Neaton, K. M. Rabe, and D. Vanderbilt, *Phys. Rev. B* **71**, 024102 (2005).
- ³² E.-M. Choi, Y.-H. Yoon, S. Lee, and H. Kang, *Phys. Rev. Lett.* **95**, 085701 (2005).
- ³³ D. Vanderbilt, *Phys. Rev. B* **32**, 8412 (1985).
- ³⁴ D. Vanderbilt and R. D. King-Smith, *cond-mat/9801177* (2005).
- ³⁵ According to the modern theory of polarization, only differences of $\langle P \rangle$ between two states of the system connected by a continuous transformation are observable quantities, while the absolute value of $\langle P \rangle$ is only defined modulo a *quantum of polarization*⁷. The condition $x_n^{\mathbf{k}^{\perp}} \in [-L/2, L/2]$ (with the metallic slab approximately centered in the origin), is important to ensure that all fractionally occupied state belong to the same supercell; in this case it is easy to show that $\langle P \rangle$ is well defined and has the same properties as in the insulating case.
- ³⁶ The $F_n(\mathbf{r})$ are constructed in reciprocal space in order to avoid Fourier aliasing errors and preserve analytical gradients.